Chemical Engineering Journal 143 (2008) 147–160

Contents lists available at ScienceDirect

Chemical Engineering Journal

journal homepage: www.elsevier.com/locate/cej

CFD and experimental studies of solids hold-up distribution and circulation patterns in gas–solid fluidized beds

G.N. Ahuja, A.W. Patwardhan*

Chemical Engineering Department, Institute of Chemical Technology, Matunga, Mumbai 400019, India

ARTICLE INFO

Article history:
Received 27 June 2007
Received in revised form 14 March 2008
Accepted 14 March 2008

Keywords:
Gas–solid fluidized bed
Euler–Euler two-fluid model
CFD
Gamma ray attenuation
Solids hold-up

ABSTRACT

The hydrodynamics of a gas–solid fluidized bed was studied using a combination of experiments and CFD simulations. Experiments were conducted with polypropylene particles (710–1000 μm in diameter) as solid phase and air as gas phase. A multifluid Eulerian model incorporating the kinetic theory for solid particles is used to simulate the gas–solid flow. Momentum exchange coefficient was calculated using the Gidaspow drag model. Effects of gas velocity, type of sparger, presence of draft tube on solid hold-up distribution and solid circulation pattern have been investigated. The presented experimental data and comparison with CFD predictions provide useful basis for further work on understanding bubbling fluidized beds.

1. Introduction

Fluidized beds are used in chemical, petroleum, pharmaceutical, metallurgical, biochemical, power generation and food industries in large scale operations, e.g. manufacturing of polypropylene and polyethylene, coating, granulation, drying, roasting, and synthesis of fuels and chemicals. Despite their widespread application, much of the development and design of fluidized bed reactors has been empirical due to the complex behavior of gas–solid flow in these systems. For any gas–solid catalyzed reaction being carried out in a fluidized bed reactor, efficient gas–solid contacting is of prime importance. Gas–solid fluidized bed reactors when operated at superficial gas velocities above the minimum fluidization velocity limit the contact of solid particles with the reactant gas due to the escape of excess gas through the reactor in the form of gas bubbles and this leads to poor gas–solid contacting. Particles even of same size are known to have different lengths of stay in the bed. Moreover, if solids undergo size changes (growth and shrinkage) a wider size distribution of solids is created within the bed giving rise to long and non-uniform residence times of solids in the reactor. So a better understanding of the dynamics of fluidized beds is a key issue in making improvements in efficiency, which can be achieved through numerical modeling. Computational fluid dynamics (CFD) is an emerging technique and holds great potential in providing detailed information of the complex fluid dynamics. It is widely applied in industry to support engineering design for single-phase systems and has become a fundamental component of research in multiphase systems, including fluidization.

2. Previous work

Several approaches have been used in the past to simulate the fluidized bed. Krishna and van Baten [1] have proposed the use of "pseudo-fluids" wherein the emulsion phase and bubble phase are defined as two fluids. Physical properties are assumed for the emulsion phase, and empirical correlations are used for rise velocity of the bubbles. These empirical parameters like emulsion density, viscosity need to be fitted to match the experimental data and hence these models are not predictive in nature. Extension of these models to systems other than those investigated is also not possible.

In the Eulerian–Eulerian approach, gas and emulsion phases are assumed to be continuous and fully interpenetrating in each control volume. Both phases are described in terms of separate conservation equations for mass and momentum. In order to couple the two momentum balances, models for the inter-phase forces are required. The inter-phase forces include drag force, lift force and the virtual mass force. Due to large difference between the emulsion phase and the fluid-phase densities, forces other than drag force are less significant, and thus can be neglected. Consequently, in most of the studies, whenever the inter-phase forces were dealt with, only drag force has been considered. The inter-phase momentum transfer is an important term in the modeling of the gas–particle interaction, since particle fluidization results from the drag exerted by the interstitial gas on the particulate phase. Taghipour et al. [2]

* Corresponding author. Tel.: +91 22 24145616; fax: +91 22 24145614.
E-mail address: awp@udct.org (A.W. Patwardhan).

1385-8947/$ – see front matter © 2008 Elsevier B.V. All rights reserved.
doi:10.1016/j.cej.2008.03.011

Nomenclature

A_t	cross-sectional area of the bed (m^2)
Ar	Archimedes number
C_D	drag coefficient
d_p	particle diameter based on screen analysis (m)
$\bar{\bar{D}}_i$	strain rate tensor for phase i (s^{-1})
e	coefficient of restitution
g	gravitational constant (m/s^2)
g_0	radial distribution function
h	axial location (m)
H	height of the bed (m)
I_G	transmitted intensity through the gas phase (s^{-1})
I_S	transmitted intensity through the solid phase (s^{-1})
I_{TP}	transmitted intensity through the two phase (s^{-1})
I_0	intensity of incident radiation (s^{-1})
L_m	height of fixed bed
L_{mf}	height of bed at minimum fluidization
P	gas-phase pressure (N/m^2)
P_s	particulate phase pressure (N/m^2)
r	radial location (m)
R	radius of the bed (m)
Re_p	particle Reynolds number
t	total thickness of the medium (m)
t_G	total thickness of the gas medium (m)
t_S	total thickness of the solid medium (m)
U_{mf}	minimum fluidization velocity (m/s)
U_t	terminal velocity of a falling particle (m/s)
U_t^*	dimensionless terminal velocity of a falling particle (m/s)
U^*	dimensionless particle velocity (m/s)
U_0	superficial gas velocity (m/s)
W	mass of solids in the bed (kg)

Greek letters

β	inter-phase drag coefficient (kg/m^3 s)
ε_g	voidage of gas phase
ε_{gmf}	voidage of gas phase at minimum fluidization
ε_{mf}	voidage in the bed at minimum fluidization
ε_s	voidage of solid phase
ε_{smf}	voidage of solid phase at minimum fluidization
ϕ_s	sphericity of a particle
Φ	angle of internal friction
γ	dissipation of granular energy (kg/m^3 s)
κ	solids thermal conductivity (kg/ms)
λ_{mfp}	mean free path (m)
λ_s	the solid bulk viscosity (g/m s)
μ_g	viscosity of gas (kg/m s)
μ_G	linear attenuation coefficient of gas (m^{-1})
μ_s	solid shear viscosity (kg/m s)
μ_S	linear attenuation coefficient of solid (m^{-1})
Θ_s	granular temperature (m^2/s^2)
ρ_g	density of gas phase (kg/m^3)
ρ_s	density of solid phase (kg/m^3)
$\bar{\bar{\tau}}$	viscous stress tensor (N/m^2)
υ	velocity vector (m/s)

Subscripts

col	collision
fr	friction
g	gas phase
kin	kinetic
max	maximum
p	particle
s	solid

Superscripts

T	transpose

have compared three drag coefficients viz. Syamlal and O'Brien [3], Gidaspow [4] and Wen and Yu [5] and found them "qualitatively similar". Similarly Pugsley and McKeen [6] have compared four drag coefficients viz. Syamlal and O'Brien [3], Gidaspow [4], Ergun [7] and Gibilaro et al. [8] at a fixed relative velocity of 0.1 m/s. At this relative velocity, the models show significant deviations at low voidage for the Syamlal and O'Brien drag model [3]. For dense-phase systems, Krishna et al. [9] showed that in case of Syamlal and O'Brien [3] model, predicted values of pressure drop and bed expansion were lower. Krishna et al. [9] and Du et al. [10] have used the Gidaspow [4] drag model for dense gas–solid systems.

When solving the two-fluid model (TFM), a set of models, either physical or empirical, are required in order to close the system of equations. One important and difficult closure is the emulsion phase stress, i.e., normal and tangential stresses of the emulsion phase. Two approaches are currently used for treating the emulsion phase stress. The first uses a constant particle viscosity (CPV) uses a relationship for the particle–particle interaction force or emulsion phase pressure ($\nabla \cdot P_s$). The emulsion phase pressure ($\nabla \cdot P_s$) can be written as

$$\nabla \cdot P_s = G(\varepsilon)\nabla\varepsilon \quad (1)$$

Rietema and Mutsers [11] have determined the functional dependence for emulsion phase elastic modulus, $G(\varepsilon)$, by measuring the interaction of a vibrating body of wire netting with homogenously fluidized beds of catalyst particles. Gidaspow and Ettehadieh [12], Ettehadieh et al. [13] and Gidaspow [14] fitted the data to obtain an expression for the emulsion phase elastic modulus. However, numerical computations of Ettehadieh et al. [13], Gidaspow [14], Kuipers et al. [15] and Bouillard et al. [16] have shown that the $G(\varepsilon)$ fit obtained from the Rietema and Mutsers [11] data is inadequate in predictive ability. Unrealistically low voidages are predicted with this correlation.

The second approach uses the kinetic theory of granular flow (KTGF), is analogous with the kinetic theory of gases [17–20]. The macroscopic behavior of the solid phase is described by the equations that account for the energy associated with particles arising out of collisions and fluctuating motions of the particles. Solution of this equation is used to describe momentum transport within the solid phase. This model also enables taking into account variation of the energy associated (and the momentum transfer associated with it) with solid motion within the bed.

This is similar to the most widely used k–ε model for turbulence in single-phase flows. The energy associated with turbulence is used to calculate the turbulent diffusion of momentum. Therefore, this theory makes it possible to use a more fundamental approach to calculate the momentum transfer rates. Empiricism (use of constant particle viscosity, or pseudo-fluid) is avoided completely. Simulations using the KTGF model have been reported by many researchers [2,9,17,20–28]. Verification and quantitative validation using experimental data is necessary for providing a reliable and predictive model [29]. Therefore, in recent years, main emphasis has been on validating various models proposed for governing and closure equations used for simulations of gas–solid fluidized beds [9,24,30].

Kuipers et al. [24,30] have carried out simulations for free bubbling fluidized bed for Geldart B as well as D type particles. Comparison of simulation results using KTGF and CPV have been carried out. Comparison of bubble size distribution, bubble rise velocity and visible bubble flow rate with generally accepted correlations of Darton et al. [31], Lim et al. [32] and Hilligardt and Werther [33] and experimental data taken from the literature have been presented. It was observed that KGTF was able to predict the experimental data slightly better than CPV.

Mori et al. [34] has proposed a novel bubble distribution model based on the population balance of bubbles, incorporating Reynolds Transport equation for solid flow. The estimated bubble diameter and solid flow pattern in bubbling fluidized bed were compared with the experimental values in cylindrical bubbling fluidized bed.

Zhang and Reese [35] have developed a heuristic model for dense gas–solid flows in vertical pipes. The numerical solutions of radial variation of solid volume fraction and solid axial velocity from this model were compared with the published experimental data and simulation of Nieuwland et al. [36,37].

Taghipour et al. [2] have studied the hydrodynamics of gas–solid fluidized bed using multifluid Eulerian model incorporating kinetic theory for solid particles. The model predictions of time averaged solid volume fraction, bed expansion ratio, pressure drop and qualitative gas–solid flow pattern were compared with the experimentally obtained pressure drop data and local voidage calculations using reflective optical fiber probe. The model was able to qualitatively predict the experimental results. However, large errors were observed in the predictions. Errors as much as 30–50% in the prediction of bed voidage and pressure drops were reported.

Pugsley and McKeen [6] have carried out simulations for FCC particles (135–170 μm) using two-fluid CFD code Multiphase Flow with Inter-phase Exchanges (MFIX). Comparison has been made based on the bed expansion, bubble diameters and rise velocities with the experimental data collected using an electrical capacitance tomography (ECT) imaging systems. They have observed large errors between the predicted values and experimental observations. In order to reduce the errors, the drag relationship was multiplied by an empirically constant. The value of this constant was varied from 0.1 to 1.0. In spite of this, the predictions agree only qualitatively.

van Wachem et al. [38] have carried out the validation of their model by comparing the predicted values of voidage and pressure fluctuations at different gas velocities with the data of Baskakov et al. [39], Schouten and Van den Bleek [40] and Schouten et al. [41].

In most of the past studies CFD model validation is done by (a) comparing bubble growth for the initial bubble [30] and (b) comparing time averaged data [2,24,42–44]. Comparison of the CFD model predictions of radial and axial distribution of solids hold-up in bubbling fluidized bed and the effect of geometrical parameters such as internals (draft tube) and gas distributor configuration (complete and partial sparging) has not been presented in the past. The effects of the above parameters on the solids hold-up distribution and circulation patterns have not been studied in detail in the past. Hence, the objectives of the present work were:

1. To develop a CFD model for bubbling fluidized bed.
2. To conduct solid hold-up measurements using gamma ray tomography to determine the variation of the solid hold-up in the radial and axial directions.
3. Understand the solids circulation patterns existing in the fluidized bed using the generated solids hold-up profiles and CFD modeling.
4. Examine the effect of superficial gas velocity, internals (draft tube) and gas distributor configuration (complete and partial sparging) on the solid hold-up distribution and circulation patterns.

3. Equipment and materials

3.1. Fluidized bed

Experiments were carried out in a transparent Perspex column of internal diameter (i.d.), 0.186 m and a total height of 1.2 m. A draft tube of internal diameter, 0.10 m and total height, 0.158 m is incorporated centrally into the bed and rested on the distributor plate. Four rectangular slots of 0.03 m height separated 0.025 m from each other have been made on the periphery of the draft tube at a height of 0.02 m from the base of the draft tube. Four bolts on the top and bottom of the draft tube help to keep it in the required position. The draft tube can be removed from the bed to make it a conventional fluidized bed. The height of the freeboard region of the bed is enough to prevent entrainment of the particles with the outgoing gas. A flat perforated plate distributor having holes each of 0.002 m i.d. is used at the bottom of the bed. The distributor plate perforated with 504 holes was used for complete sparging whereas the one with 50 holes was used for partial sparging. The distributor plate was covered by a 100 μm screen to support the bed.

A schematic diagram of the fluidized bed set-up is shown in Fig. 1. Compressed air from the compressor controlled by a valve and routed through a rotameter (for flow measurement) was used as the gas phase to fluidize the solids. The different parameters characterizing the properties of the solid particles were either measured experimentally and/or calculated. The accurate determination of these properties was necessary for fixing the experimental conditions such as gas velocity and thus the regime of operation.

3.2. Material property estimation

The solid particles used in the present study were in the size range of 710–1000 μm. Sieve analysis of the feed was carried out and the mean particle size (d_p) of the particles was calculated based on the size distribution. The mean particle size was found to be 853 μm. The density of the particles (polypropylene) was taken to be 906 kg/m^3. The value of particle sphericity was assumed to be equal to one.

Pressure drop across the bed (Δp_b) was measured first by increasing and then decreasing the air flow rate (superficial air velocity). A plot of Δp_b vs. U_0 was made, and this was used to determine the minimum fluidization velocity (U_{mf}). The value of U_{mf} was found to be 0.176 m/s. This value of U_{mf} was used in the Ergun equation:

$$\frac{\Delta p_b}{L_m} = 150\frac{(1-\varepsilon)^2}{\varepsilon^3}\frac{\mu_g \times u_0}{(\phi_s d_p)^2} + 1.75\frac{1-\varepsilon}{\varepsilon^3}\frac{\rho_g u_0^2}{\phi_s d_p} \quad (2)$$

The onset of fluidization (drag force by upward moving gas balanced by the weight of the particles) is expressed by

$$\Delta p_b A_t = W = A_t L_{mf}(1-\varepsilon_{mf}) \times (\rho_s - \rho_g)g \quad (3)$$

Rearranging Eq. (3), at minimum fluidization conditions, we have

$$\frac{\Delta p_b}{L_{mf}} = (1-\varepsilon_{mf}) \times (\rho_s - \rho_g)g \quad (4)$$

At minimum fluidization conditions, Eq. (2) can be written as

$$\frac{\Delta p_b}{L_{mf}} = 150\frac{(1-\varepsilon_{mf})^2}{\varepsilon_{mf}^3}\frac{\mu_g \times U_{mf}}{(\phi_s d_p)^2} + 1.75\frac{1-\varepsilon_{mf}}{\varepsilon_{mf}^3}\frac{\rho_g U_{mf}^2}{\phi_s d_p} \quad (5)$$

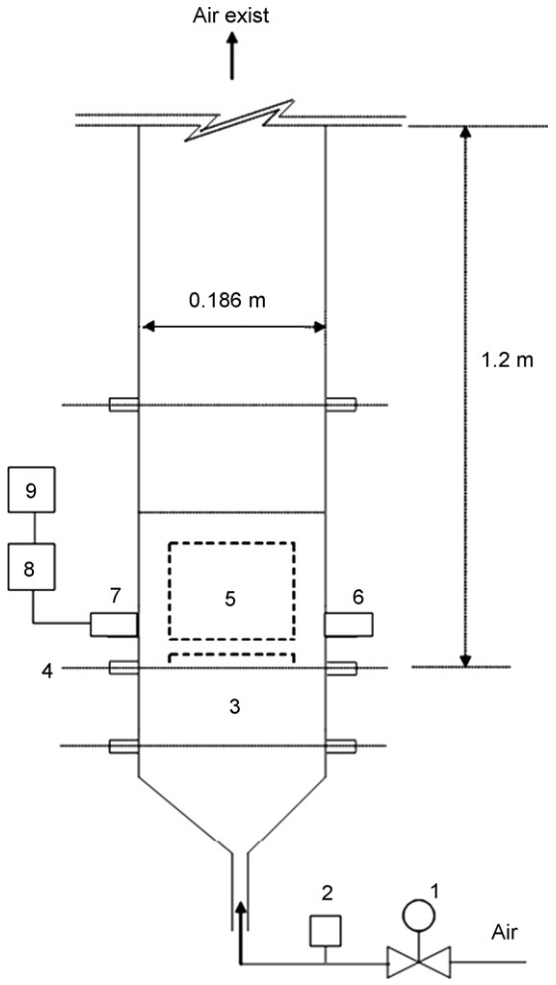

Fig. 1. Schematic diagram of experimental set-up used for tomography measurements in a gas–solid fluidized bed: (1) air flow regulator, (2) air rotameter, (3) calming section, (4) distributor plate, (5) draft tube, (6) radioactive source, (7) detector, (8) data acquisition system and (9) personal computer.

Equating Eqs. (4) and (5), and using the values of the mean particle size (d_p) of 853 μm, particle density (ρ_s) of 906 kg/m^3, air density (ρ_g) of 1.18 kg/m^3, air viscosity (μ_g) of 1.8×10^{-5} kg/m s, sphericity (ϕ_s) of one, and L_{mf} (height of bed at minimum fluidization conditions) of 0.186 m and solving for ε_{mf}, the bed voidage at minimum fluidization was found to be 0.378.

The calculation of the terminal settling velocity (U_t) was important in order to know the limit up to which the superficial gas velocity can be increased without causing carry-over of solids. Also, as it was necessary to operate the bed under bubbling regime, an accurate estimation was important in order to fix the operating conditions. Using d_p as the smallest size of solids actually present in the appreciable quantities in the bed (710 μm in the present case), d_p^* was calculated using the following equation

$$d_p^* = d_p \left[\frac{\rho_g(\rho_s - \rho_g)}{\mu_g^2} \right]^{1/3} \quad (6)$$

Using the value of d_p^*, U_t^* was calculated using the equation shown below

$$U_t^* = \left[\frac{18}{(d_p^*)^2} + \frac{2.335 - 1.744\phi_s}{(d_p^*)^{0.5}} \right]^{-1} \quad (7)$$

Table 1
Bed material properties

Parameter	Unit	Value
Particle size range	μm	710–1000
Mean particle size	μm	853
Particle density	kg/m^3	906
Voidage at minimum fluidization condition (ε_{mf})	–	0.378
Sphericity (ϕ_s)	–	1
Minimum fluidization velocity (U_{mf})	m/s	0.176
Terminal settling velocity (U_t)	m/s	3.06

The value of terminal settling velocity is obtained by solving the equation given below using the values of d_p^* and U_t^*.

$$U_t^* = U_t \left[\frac{\rho_g^2}{\mu_g(\rho_s - \rho_g)g} \right]^{1/3} \quad (8)$$

The terminal settling velocity for the solid particles under consideration was found to be 3.06 m/s. The value of d_p^* ($Ar^{1/3}$) for d_p of 853 μm was calculated to be 27.16. At U_0 of 0.99 m/s and 2.19 m/s, the values of U^* were calculated to be 2.03 and 4.5, respectively. Using the plot of $U^*(U_t^*)$ vs. $Ar^{1/3}$ (d_p^*) proposed by Grace [45], it was found that the bed if operated at U_0 of 0.99 m/s and 2.19 m/s, would behave as a bubbling bed. The solid material properties have been summarized in Table 1.

3.3. Gamma ray tomography

The experimental set-up used for the tomographic measurements of solid hold-up is shown in Fig. 1. It consists of a 1 milliCurie ^{137}Cs γ-source and sodium iodide with thallium-activated scintillation (BICRON) detectors positioned on either side of the column (bed). The related hardware and software (photomultiplier tube, preamplifier, 8 channel analyzer, and data acquisition system) are same as those discussed by Thatte et al. [46]. Both the source and detectors were collimated with lead. Both the collimators were cylindrical, 0.046 m in diameter and 0.0103 m long. The collimator slit was 0.02 m in length and 0.002 m in width.

3.4. Experimental measurements and procedure

The experimental set-up as shown in Fig. 1 allowed flexibility to study the effect of a number of parameters such as presence and absence of draft tube and sparger/distributor configuration. Experiments were carried out for two different conditions viz. (i) with and without a draft tube and (ii) complete and partial sparging. In the case of complete sparging, measurements were carried out at (U_0/U_{mf}) values of 5.6 and 12.4, whereas, in the case of partial sparging, only measurements at (U_0/U_{mf}) of 12.4 were conducted. Axial locations for the measurements were selected so as to allow hold-up measurements along the entire length of the fluidized bed (i.e., just above the distributor, within the bed and below the bed surface). These locations correspond to h/H of 0.25, 0.58 and 0.89, respectively. A summary of the experimental conditions for the present study has been given in Table 2A. Table 2B compares the

Table 2A
Summary of experimental conditions

Case	Geometrical conditions		Parameters varied, U_0/U_{mf}
	Draft tube	Type of sparging	
A	–	Complete	5.6 and 12.4
B	–	Partial	12.4
C	Present	Complete	5.6 and 12.4
D	Present	Partial	12.4

Table 2B
Comparison of the geometry and operating conditions in this work with published literature

Author	Diameter of vessel, D (mm)	H/D	U_0/U_{mf}
Taghipour et al. [2]	280	1.43	0.5–6
Pugsley and McKeen [6]	140	3.42	14.3, 28.6, 42.3, 57.1
Pain et al. [22]	382	1.33	14.3
Johansson et al. [27]	300	2	1.3
Van Wachem et al. [38]	200–400	1.7–0.85	1–4
Katsuya and Takashi [61]	150	1	2, 3, 4, 6
Ouyang and Li [67]	300	2	1.75
Gera et al. [72]	600	0.9	16.67
Gamwo et al. [73]	406	2	1
Current work	186	1	5.6 and 12.4

geometry and operating conditions in the present work with those reported in the previous literature.

Typical industrial fluidized beds operate in the range of five to ten times the minimum fluidization velocity. Therefore, these two values of superficial gas velocity were chosen. The bed height (H/D) was kept 1, as there are many industrial cases (hydrometallurgical operations and fluid bed dryers) that are operated as shallow beds. The effect of sparger type would also be most pronounced in the near sparger region and therefore shallow beds have been considered.

Parallel beam scanning method was employed and scans were carried out at 9 radial locations for each axial position ($h/H = 0.25$, 0.58 and 0.89). The number of events and dwell time were fixed at 20 and 10 s, respectively. The total acquisition time for each line plane (chord) measurement was 200 s. The two-phase counts were checked with the background counts. Every measurement yielded the value of chordal solid hold-up. Scans were performed on an empty bed, a bed filled with solids in a known packed bed (static) condition and on a bed under operating conditions. These three measurement values were used to calculate the line averaged solids hold-up for each chord. The solids hold-up was calculated using the three counts (air, solid and two phase) as follows.

The intensity I_G, after travel through air of thickness t is given as

$$I_G = I_O \cdot \exp[-\mu_G t] \tag{9}$$

The intensity I_S, after travel through a packed bed of solids of thickness t is given as

$$I_S = I_O \cdot \exp[-(\mu_S t_S + \mu_G t_G)] \tag{10}$$

Substituting for t_S and t_G,

$$I_S = I_O \cdot \exp\lfloor -(\mu_S t \varepsilon_{smf} + \mu_G t \varepsilon_{gmf})\rfloor \tag{11}$$

Putting $\varepsilon_{gmf} = 1 - \varepsilon_{smf}$

$$I_S = I_O \cdot \exp\lfloor -(\mu_S t \varepsilon_{smf} + \mu_G t(1 - \varepsilon_{smf}))\rfloor \tag{12}$$

For the case of fluidized bed, similar approach gives the following equation:

$$I_{TP} = I_O \cdot \exp[-(\mu_G t(1 - \varepsilon_s) + \mu_S t \varepsilon_s)] \tag{13}$$

From Eqs. (9) and (12),

$$\ln\left(\frac{I_S}{I_G}\right) = -\mu_S t \varepsilon_{smf} - \mu_G t(1 - \varepsilon_{smf}) - [-\mu_G t] \tag{14}$$

Simplifying,

$$\ln\left(\frac{I_S}{I_G}\right) = \mu_G t \varepsilon_{smf} - \mu_S t \varepsilon_{smf} \tag{15}$$

$$\ln\left(\frac{I_S}{I_G}\right) = (\mu_G - \mu_S) t \varepsilon_{smf} \tag{16}$$

From Eqs. (9) and (13),

$$\ln\left(\frac{I_{TP}}{I_G}\right) = -\mu_S t \varepsilon_s - \mu_G t(1 - \varepsilon_s) - [-\mu_G t] \tag{17}$$

Simplifying,

$$\ln\left(\frac{I_{TP}}{I_G}\right) = \mu_G t \varepsilon_s - \mu_S t \varepsilon_s \tag{18}$$

$$\ln\left(\frac{I_{TP}}{I_G}\right) = (\mu_G - \mu_S)\varepsilon_s t \tag{19}$$

From Eqs. (16) and (19),

$$\frac{\ln\left[I_{TP}/I_G\right]}{\ln\left[I_S/I_G\right]} = \frac{\varepsilon_s}{\varepsilon_{smf}} \tag{20}$$

Eq. (20) was used to calculate the chordal solid hold-up using the three counts (air, solid and two phase).

In the present work, the emphasis was on measuring the axial and radial gradients of solid fraction. Further, due to large time required for measuring tangential symmetry could be assumed. In view of this, the Abel transform method explained in Shollenberger et al. [47], already applied for calculation of local gas hold-up in stirred tanks by Thatte et al. [46] has been used for the calculation of local solid hold-ups.

3.5. CFD model

This section describes the modeling equations employed in the present Euler–Euler two-fluid CFD model.

Continuity equation for the fluid phase

$$\frac{\partial(\varepsilon_g \rho_g)}{\partial t} + \nabla \cdot (\varepsilon_g \rho_g v_g) = 0 \tag{21}$$

Continuity equation for the emulsion phase

$$\frac{\partial(\varepsilon_s \rho_s)}{\partial t} + \nabla \cdot (\varepsilon_s \rho_s v_s) = 0 \tag{22}$$

Momentum equation for the fluid phase

$$\frac{\partial(\varepsilon_g \rho_g v_g)}{\partial t} + \nabla \cdot (\varepsilon_g \rho_g v_g v_g) = \nabla \cdot \bar{\bar{\tau}}_g + \varepsilon_g \rho_g g - \varepsilon_g \nabla \cdot P - \beta(v_g - v_s) \tag{23}$$

Momentum equation for the emulsion phase

$$\frac{\partial(\varepsilon_s \rho_s v_s)}{\partial t} + \nabla \cdot (\varepsilon_s \rho_s v_s v_s) = \nabla \cdot \bar{\bar{\tau}}_s + \varepsilon_s \rho_s g - \nabla \cdot P_s - \varepsilon_s \nabla \cdot P + \beta(v_g - v_s) \tag{24}$$

$$\bar{\bar{\tau}}_i = 2\mu_i \bar{\bar{D}}_i + \left(\lambda_i - \frac{2}{3}\mu_i\right) \cdot \mathrm{tr}(\bar{\bar{D}}_i)\bar{\bar{I}} \tag{25}$$

$$\bar{\bar{D}}_i = \tfrac{1}{2}[\nabla \cdot v_i + (\nabla \cdot v_i)^T] \tag{26}$$

The inter-phase momentum transfer is an important term in the modeling of the gas–particle interaction. The drag force acting on a particle in fluid–solid systems can be represented by the product of a momentum transfer coefficient, β and the slip velocity $(v_g - v_s)$ between the two phases [48,49]. Gidaspow [4] drag model, has been used in the present work. Gidaspow [4] assume that Ergun [7] equation to be valid for the fluidized conditions ($\varepsilon_g < 0.8$). The Gidaspow [4] model assumes that when the gas fraction is more than 0.8, it can be considered to be a gas bubble phase. The momentum exchange can then be considered to be between that of a bubble surrounded by emulsion. The momentum exchange under such conditions is obtained from the correlation of Wen and Yu [5] (Eqs. (27), (29) and (30)). At lower values of gas fraction, the momentum exchange can

be considered to be between that of the gas and surrounding dense phase of emulsion. The momentum transfer under such conditions can be considered to be given by Ergun equation (Eq. (28)):

$$\beta = \frac{3C_D\varepsilon_s\varepsilon_g\rho_g|v_g - v_s|}{4d_p}\varepsilon_g^{-2.65}, \quad \varepsilon_g \geq 0.8 \tag{27}$$

$$\beta = 150\frac{\varepsilon_s^2\mu_g}{\varepsilon_g d_p^2} + 1.75\frac{\varepsilon_s\rho_g|v_g - v_s|}{d_p}, \quad \varepsilon_g < 0.8 \tag{28}$$

$$C_D = \frac{24}{Re_p}[1 + 0.15(Re_p)^{0.687}] \tag{29}$$

$$Re_p = \frac{\varepsilon_g\rho_g d_p|v_g - v_s|}{\mu_g} \tag{30}$$

Using these equations, it becomes possible to calculate the momentum exchange at any point in the bed.

3.6. Kinetic theory of granular flow

The two-fluid model also requires constitutive equations to describe the rheology of the particulate solid phase, i.e., the particulate phase viscosity and the particulate phase pressure gradient. When the particle motion is dominated by collisional interactions, concepts from gas kinetic theory [18] can be used to describe the effective stresses in the solid phase resulting from particle streaming (kinetic contribution and direct collisions) collisional contribution. Constitutive relations for the solid-phase stress based on kinetic theory concepts have been derived by Lun et al. [19], allowing for the inelastic nature of particle collisions. Analogous to the thermodynamic temperature for gases, the granular temperature can be introduced as a measure of the particle velocity fluctuations.

$$\Theta_s = \tfrac{1}{3}\overline{v'^2_s} \tag{31}$$

Since the solid-phase stress depends on the magnitude of these particle-velocity fluctuations, a balance of the granular energy $(3/2)\Theta_s$ associated with these particle-velocity fluctuations is required to supplement the continuity and momentum balance for both phases. This balance is given as:

$$\frac{3}{2}\left[\frac{\partial}{\partial t}(\varepsilon_s\rho_s\Theta_s) + \nabla\cdot(\varepsilon_s\rho_s\Theta_s v_s)\right]$$
$$= (-\nabla\cdot P_s\bar{\bar{I}} + \tau_s) : \nabla v_s + \nabla\cdot(k_s\nabla\Theta_s) - \gamma_s + \Phi_\Theta \tag{32}$$

where the first term on the right hand side represents the creation of fluctuating energy due to shear in the particle phase, the second term represents the diffusion of fluctuating energy due to gradients in Θ_s, γ_s represents the dissipation due to inelastic particle–particle collisions. This term is represented by the expression derived by Lun et al. [19].

$$\gamma_s = 12(1 - e^2)\frac{\varepsilon_s^2\rho_s g_0}{d_s\sqrt{\pi}}\Theta_s^{3/2} \tag{33}$$

and Φ_Θ represents the exchange of fluctuating energy between gas and solid phase and is calculated according to expression of Ding and Gidaspow [20]. This accounts for the loss of granular energy due to friction with the gas.

$$\Phi_\Theta = -3\beta\Theta_s \tag{34}$$

Rather than solving the complete granular energy balance given in Eq. (32), some researchers [25,38,50,51] assume the granular energy is in a steady state and dissipated locally, and neglect convection and diffusion. Boemer et al. [52] have carried out simulations using three granular temperature models (i.e., constant, algebraic expression and partial differential equation), and compared the simulated results with the experiments of Kuipers [53]. It was found that all the three simulations give similar results. This means it is possible to simplify the differential Eq. (32) by retaining only the generation and the dissipation terms. Eq. (32) simplifies to an algebraic expression for the granular temperature:

$$0 = (-\nabla\cdot P_s\bar{\bar{I}} + \tau_s) : \nabla v_s - \gamma_s \tag{35}$$

Because the generation and dissipation terms dominate in dense-phase flows, it is anticipated that this simplification is a reasonable one in dense regions of flow.

3.7. Solid-phase stress tensor

The solid pressure represents the normal solid-phase forces due to particle–particle interactions. Solid pressure given by Lun et al. [19] is

$$P_s = \rho_s\varepsilon_s\Theta_s + 2g_0\varepsilon_s^2\rho_s\Theta_s(1 + e) \tag{36}$$

The first part of the solids pressure represents the kinetic contribution, and the second part represents the collisional contribution. The kinetic part of the stress tensor physically represents the momentum transferred through the system by particles moving across imaginary shear layers in the flow; the collisional part of the stress tensor denotes the momentum transferred by direct collisions.

The solids bulk viscosity describes the resistance of the particle suspension against compression. Solid bulk viscosity given by Lun et al. [19] is

$$\lambda_s = \frac{4}{3}\varepsilon_s^2\rho_s d_p g_0(1 + e)\sqrt{\frac{\Theta_s}{\pi}} \tag{37}$$

Table 3
Solids shear viscosity

Lun et al. [19]	$\mu_s = \frac{4}{5}\varepsilon_s^2\rho_s d_p g_0(1+e)\sqrt{\frac{\Theta_s}{\pi}} + \frac{1}{15}\sqrt{\Theta\pi}\frac{\rho_s d_s g_0\varepsilon_s^2(1+e)(3/2e-1/2)}{3/2-1/2e} + \frac{1}{6}\sqrt{\Theta\pi}\frac{\rho_s d_s\varepsilon_s(3/4e-1/4)}{3/2-1/2e} + \frac{10}{96}\sqrt{\Theta\pi}\frac{\rho_s d_s(3/2e-1/2)}{g_0(1+e)(3/2-1/2e)}$
Syamlal et al. [50]	$\mu_s = \frac{4}{5}\varepsilon_s^2\rho_s d_p g_0(1+e)\sqrt{\frac{\Theta_s}{\pi}} + \frac{1}{15}\sqrt{\Theta\pi}\frac{\rho_s d_s g_0\varepsilon_s^2(1+e)(3/2e-1/2)}{3/2-1/2e} + \frac{1}{12}\sqrt{\Theta\pi}\frac{\rho_s d_s\varepsilon_s}{3/2-1/2e}$
Gidaspow [4]	$\mu_s = \frac{4}{5}\varepsilon_s^2\rho_s d_p g_0(1+e)\sqrt{\frac{\Theta_s}{\pi}} + \frac{1}{15}\sqrt{\Theta\pi}\rho_s d_s g_0\varepsilon_s^2(1+e) + \frac{1}{6}\sqrt{\Theta\pi}\rho_s d_s\varepsilon_s + \frac{10}{96}\sqrt{\Theta\pi}\frac{\rho_s d_s}{g_0(1+e)}$
Hrenya and Sinclair [54]	$\mu_s = \frac{4}{5}\varepsilon_s^2\rho_s d_p g_0(1+e)\sqrt{\frac{\Theta_s}{\pi}} + \frac{1}{15}\sqrt{\Theta\pi}\frac{\rho_s d_s g_0\varepsilon_s^2(1+e)(3/2e-1/2)}{3/2-1/2e} + \frac{1}{6}\sqrt{\Theta\pi}\frac{\rho_s d_s\varepsilon_s(1/2(1+(\lambda_{mfp}/R))+3/4e-1/4)}{(1+(\lambda_{mfp}/R))(3/2-1/2e)} + \frac{10}{96}\sqrt{\Theta\pi}\frac{\rho_s d_s}{g_0(1+(\lambda_{mfp}/R))(1+e)(3/2-1/2e)}$

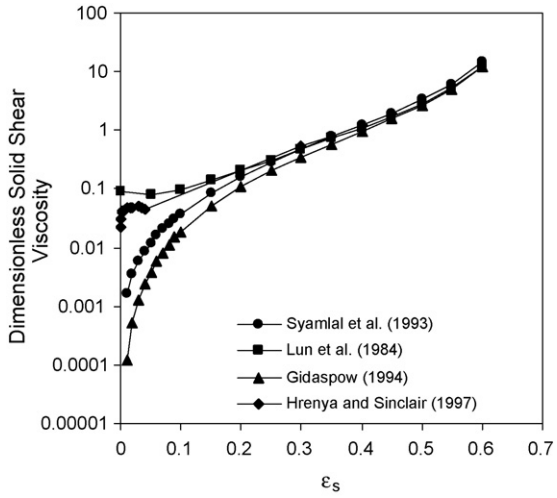

Fig. 2. Comparison of solid shear viscosity from different kinetic theory models; $e = 0.95$ and $\varepsilon_{smax} = 0.65$.

The solids shear viscosity contains shear viscosity arising from particle momentum exchange due to translation and collision. The collisional and kinetic parts, and the optional frictional part, are added:

$$\mu_s = \mu_{s,col} + \mu_{s,kin} + \mu_{s,fr} \tag{38}$$

However, the kinetic theory description for the solids shear viscosity often differs between the various two-fluid models. Table 3 gives different expressions that have been used to compute the solid shear viscosity. Fig. 2 shows a comparison of the constitutive models for the dimensionless solids shear viscosity ($\mu_s/d_p\rho_s\sqrt{\Theta_s}$) as a function of the solid volume fraction. For ε_s of 0.6, the value of solids shear viscosity is 1.7 Pa s (about 1000 times of liquids). This indicates the high level of momentum exchange between the gas bubbles and emulsion and the rapid decay of momentum in the emulsion phase. All the models yield practically the same solids shear viscosity at $\varepsilon_s > 0.25$. When the solid volume fraction is below 0.2, the models start deviating from one another. Gidaspow [4] does not account for the inelastic nature of particles in the kinetic contribution of the total stress, as Lun et al. [19] do, claiming this correction is negligible. Hrenya and Sinclair [54] follow Lun et al. [19] model, but constrain the mean free path of the particle by a dimension characteristic of the actual physical system. This is opposed to the theory of Lun et al. [19], which allows the mean free path to tend toward infinity. The solids viscosities in case of Lun et al. [19], tends toward a finite value as the solid volume fraction tends to zero, which is not correct. Hence, by constraining the mean free path, the limit of the Hrenya and Sinclair [54] shear viscosity expression correctly tends to zero as the solid volume fraction approaches zero. For $\varepsilon_s > 0.05$, there is no difference in the predicted solids viscosity of Lun et al. [19] and Hrenya and Sinclair [54]. The solids shear viscosity of Syamlal et al. [50] neglects the kinetic or streaming contribution, which dominates in dilute-phase flow. This is a reasonable assumption for dense suspensions such as bubbling fluidized beds. The Syamlal et al. [50] solids shear viscosity also tends to zero as the solid volume fraction tends to zero. In this case, however, this solids shear viscosity limit is reached because the kinetic contribution to the solids viscosity is neglected. The models of Symalal et al. [50] and Gidaspow [4] predict a continuous decrease in the viscosity with a reduction in the solid volume fraction. The decrease in viscosity is more rapid as volume fraction of zero approaches. Both these models behave in a similar manner. The model of Lun et al. [19] predicts a constant value at volume fraction of zero. The model of Hrenya and Sinclair [54] shows a decrease in viscosity till volume fraction of 0.05. A further decrease in solid volume fraction causes a marginal increase in the viscosity.

Table 4
Radial distribution function

Carnahan and Starling [56]	$g_0 = \frac{1}{1-\varepsilon_s} + \frac{3\varepsilon_s}{2(1-\varepsilon_s)^2} + \frac{\varepsilon_s^2}{2(1-\varepsilon_s)^3}$
Lun and Savage [57]	$g_0 = \left[1 - \left(\frac{\varepsilon_s}{\varepsilon_{smax}}\right)^{-2.5\varepsilon_{\varepsilon_{smax}}}\right]$
Sinclair and Jackson [58]	$g_0 = \left[1 - \left(\frac{\varepsilon_s}{\varepsilon_{smax}}\right)^{1/3}\right]^{-1}$
Gidaspow [4]	$g_0 = \frac{3}{5}\left[1 - \left(\frac{\varepsilon_s}{\varepsilon_{smax}}\right)^{1/3}\right]^{-1}$

In the kinetic theory, only the kinetic and collisional contributions to the internal momentum transport of the particulate suspension are accounted for. All the collisions are assumed to be binary and quasi-instantaneous. In regions with high particle volume fractions, multi-particle contacts (frictional effects) dominate the stress generation mechanism. In long-term contacts much more energy will be dissipated which results in a self-enhancing mechanism for the formation of extremely dense regions, since these particles have hardly any energy left to escape these regions [24,30]. It is therefore necessary to account for the frictional stresses in the model. In the present work Schaffer [55] frictional stress is used.

$$\mu_{s,fr} = \frac{P_s \sin\phi}{2\sqrt{I_{2D}}} \tag{39}$$

where P_s is the solids pressure, ϕ is the angle of internal friction, and I_{2D} is the second invariant of the deviatoric stress.

3.8. Radial distribution function

The solid-phase stress is dependent on the radial distribution function at contact. The various forms of the radial distribution function are given in Table 4 and are plotted in Fig. 3 as a function of the solid volume fraction. Lun et al. [19] employed the Carnahan and Starling [56] expression for the radial distribution function. The Car-

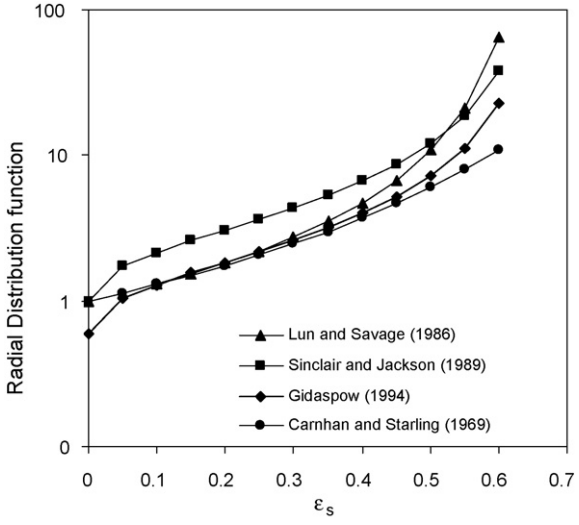

Fig. 3. Comparison of radial distribution function from different model for $\varepsilon_{smax} = 0.65$.

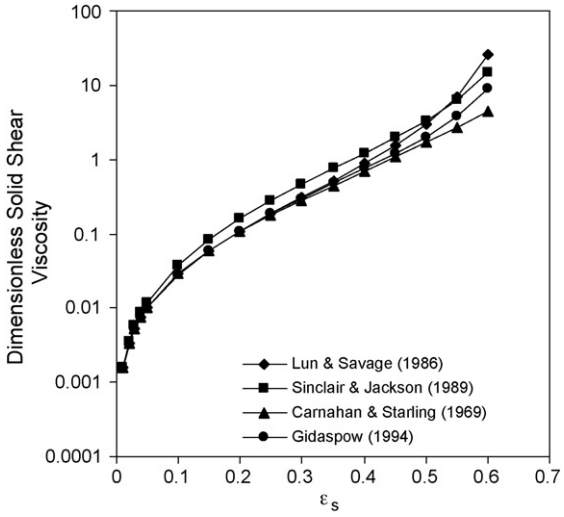

Fig. 4. Dimensionless solid shear viscosity from different radial distribution functions. Solid shear viscosity model of Syamlal et al. [50]; $e = 0.95$ and $\varepsilon_{smax} = 0.65$.

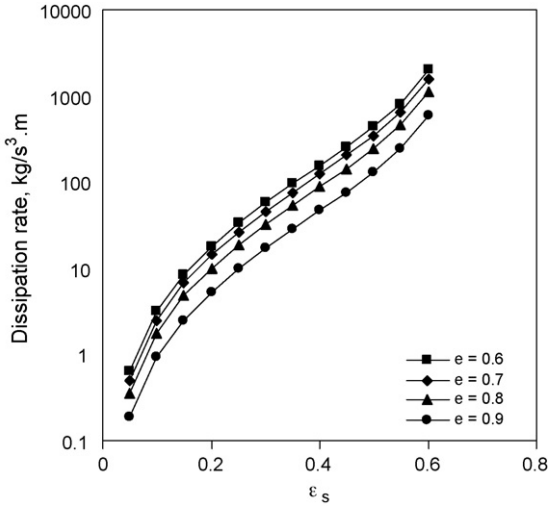

Fig. 5. Effect of restitution coefficient on dissipation rate.

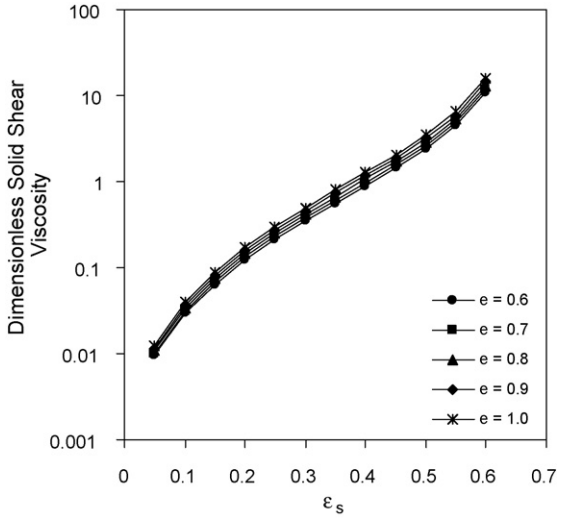

Fig. 6. Variation of dimensionless solid shear viscosity with restitution coefficient. Solid shear viscosity follows Syamlal et al. [50]; g_0 of Sinclair and Jackson [58] and $\varepsilon_{smax} = 0.65$.

nahan and Starling [56] expression, however, does not tend toward the correct limit at closest solids packing. Because particles are in constant contact at the maximum solid volume fraction, the radial distribution function at contact tends to infinity. Therefore, alternative expressions to the Carnahan and Starling [56] expression have been proposed by Gidaspow [4], Lun and Savage [57] and Sinclair and Jackson [58]. The expression of Gidaspow [4] most closely coincides with the data over the widest range of solid volume fractions. The expression of Gidaspow [4], however, does not approach the correct limit of one as the solid volume-fraction approaches zero. The expression of Sinclair and Jackson [58], approach the correct limit of one as the solid volume-fraction approaches zero.

Fig. 4 presents the effect of different expressions of the radial distribution functions on the dimensionless solids shear viscosity. Dimensionless solid shear viscosity of Syamlal et al. [50] has been plotted for restitution coefficient of 0.95 and maximum packing of 0.65. All the models yield practically the same solids shear viscosity.

Table 5
Comparison of grid sizes used in previous work

Author	Grid size in x-direction (mm), Δx	Grid size in y-direction (mm), Δy	Grid size in z-direction (mm), Δz	Number of grids in x-direction	Number of grids in y-direction	Number of grids in z-direction
Hansen et al. [64]	10	10	90	26	26	120
Ding and Gidaspow [20]	6	18	–	67	34	–
Sokolichin and Eigenberger [65]	20	27	–	25	75	–
John et al. [66]	5	5	–	30	200	–
Ouyang and Li [67]	10	20	–	61	61	–
Derek et al. [68]	5	5	5	30	30	60
Derek et al. [68]	5	5	–	30	30	–
Yang et al. [69]	2.25	35	–	40	300	–
Gidaspow and Tsuo [70]	7.62	76.2	–	10	72	–
Taghipour et al. [2]	5	5	–	56	200	–
Enwald and Almstedt [17]	5	10	–	60	224	–
Nhang and VenderHeyden [71]	6.45	6.45	13.33	31	31	150
Pugsley and McKeen [6]	2.5	2.5	–	56	400	–
Krishna and van Baten [1]	20	20	19.5	75	75	410
Krishna and van Baten [1]	6.33	6.33	18.75	30	30	160
Krishna and van Baten [1]	12.66	12.66	18.75	30	30	160
Krishna and van Baten [1]	26.66	26.66	48.15	75	75	270
Krishna and van Baten [1]	53.33	53.33	49	75	75	510
Krishna and van Baten [1]	80	80	49.29	75	75	710
Current work	1	1	–	186	900	–

3.9. Effect of restitution coefficient

The main dissipative term in the turbulent kinetic energy equation consists of dissipation due to particle–particle collision. This energy dissipation depends on the value of restitution coefficient (Eq. (33)). Fig. 5 shows the effect of restitution coefficient on the dissipation of turbulent kinetic energy of the solids. An increase in the restitution coefficient means collisions are more elastic and therefore the dissipation rate decreases. This causes the granular temperature to increase, leading to an increase in the solid shear viscosity and diffusion, resulting in smaller gradients and lesser bubbles (lower gas hold-up) [59]. This can be seen in Fig. 6.

3.10. CFD modeling strategy

A commercial grid-generation tool, GAMBIT 2.1.2 (of Fluent Inc., USA) was used to create the 2D geometry (0.186 m × 0.9 m) and generate the grids. Initially grid sensitivity studies were carried out (results not shown for the sake of brevity). Table 5 compares the grid sizes employed in this work as compared to the published literature. It can be seen that the grid sizes employed in this work are much smaller and the number of grids are much larger than those used previously. For the simulations in this study the commercial CFD code FLUENT 6.2.16 (of Fluent Inc., USA) was used. Standard k–ε model was used. "SIMPLE" scheme for pressure–velocity coupling was used. The wall was modeled using no-slip boundary conditions for both phases. The bottom of the bed was defined as velocity inlet to specify a uniform gas inlet velocity. Pressure boundary conditions were employed at the top of the freeboard, which was set to a reference value of 1.01325×10^5 Pa. The settled bed was considered 0.186 m deep and initial solids volume fraction was defined as 0.622 with a maximum packing of 0.65. The simulations were started with specifying the axial gas velocity in the settled bed region (i.e., 0.186 m) as U_0/ε_{gmf} and U_0 in the freeboard region. The inlet superficial gas velocity (U_0) was set as 5.6 and 12.4 times of U_{mf}, where U_{mf} = 0.176 m/s. The restitution coefficient which quantifies the elasticity of particle collisions (one for fully elastic and zero for fully inelastic) was taken as 0.95. 2D simulations were carried out using Euler–Euler two-fluid model with Gidaspow [4] drag model. Constitutive equations for the particulate phase properties such as solid pressure, solid bulk viscosity and the solid shear viscosity were derived from the KTGF. Models of Lun et al. [19] were used for solid pressure and granular bulk viscosity. Model of Syamlal et al. [50] was used for solid shear viscosity. Similarly, Radial distribution function of Sinclair and Jackson [58] was used, as it approaches the correct value of one as the solids volume fraction tends to zero. Model of Schaffer [55] was used for frictional stress.

3.11. CFD model validation

The only constants that appear in the KTGF model are the restitution coefficient and the radial distribution function. The radial distribution function is the equilibrium radial distribution at particle contact derived from statistical mechanics. It is a measure of the probability of inter-particle contact, which involves a constant ε_{smax} (maximum solid packing). Sensitivity study for restitution coefficient and ε_{smax} was carried out. Past studies have shown the use of 0.6–0.7 for ε_{smax}. It was observed that increase in the value of ε_{smax} for a particular value of restitution coefficient results in an increase in the solids hold-up. Change in the value of restitution coefficient significantly affects the results in numerical simulations of dense suspensions. For dense suspensions, an increase in restitution coefficient implies that collisions are more elastic. This leads to lowering of the energy dissipation rate, causing the granular temperature to increase. This in turn causes an increase of the viscosity (Fig. 6) and diffusion, resulting in smaller gradients and lesser bubbles (lower gas hold-up) [59]. For higher values of restitution coefficient (i.e., more elastic collisions), the compaction of the particles is insufficient due to the relatively high granular energy, which results in a uniform bed expansion [60]. Ranade and Utikar [23] have used a value of 0.6 for restitution coefficient for polypropylene. But it resulted in lower solids hold-up in present case. Simulations were carried out for restitution coefficient of 0.6, 0.9 and 0.95 for a constant value of ε_{smax}. It was observed that with increase in the restitution coefficient the solids hold-up increases.

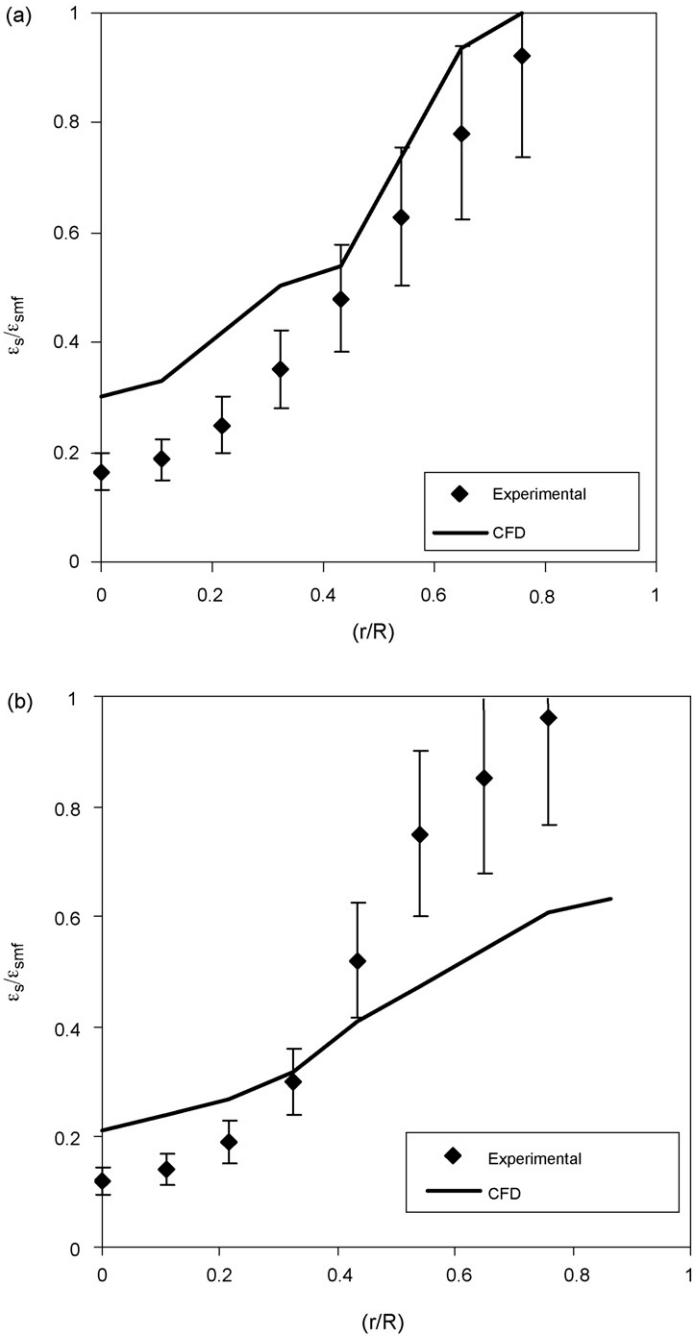

Fig. 7. Solids hold-up for partial sparging with and without draft tube for U_0/U_{mf} = 12.4 at h/H = 0.25; e = 0.95, ε_{smax} = 0.65. (a) Partial sparging with draft tube. (b) Partial sparging without draft tube.

The values of restitution coefficient and ε_{smax} were varied to obtain as good a match as possible for one of the simulations runs (Fig. 7a). It was observed that a restitution coefficient of 0.95 and ε_{smax} of 0.65 give reasonably good predictions. This Figure compares the predicted hold-up with the experimental measurements for partial sparging with draft tube. Figure shows that the solid hold-up increases with an increase in the radial distance. The solid hold-up values are lower in the centre and higher near the walls indicating that the gas bubbles are preferentially going through the central region of the bed. This is because of the nature of sparging (partial sparging) and presence of draft tube.

The phenomenon of fluidization is essentially dynamic. When a bubble is passing a point the hold-up of the solid phase is zero. When the emulsion is present the hold-up of the solid phase is close to its minimum fluidization value. Thus, when a time averaged hold-up is measured at a particular point, it is associated with its own standard deviation. Further, the hold-up values have been measured with the help of gamma ray attenuation tomography. This technique is also inherently dynamic in nature because the counts are measured based on emission of gamma rays from the source. In order to minimize the errors associated, counts have been measured for over a long period of time. Repeated measurements were carried out to quantify the errors in the measurement. The reproducibility of the data was within 20%. Error bars have been indicated in Fig. 7a and b. In order to capture, a dynamic process like gas–solid fluidized bed, one should have ideally used a dynamic, time-dependent CFD model, with the bubble phase treated in a Lagrangian manner and emulsion phase treated in an Eulerian manner. This approach is numerically too intensive due to the presence of a large number of bubbles of different sizes. The objective of the work was to understand, model (from first principles) and evaluate the effects of different types of spargers and internals on hold-up distribution and the solid circulation rates. Therefore, as a first step, steady state, two-fluid model has been developed, where both the phases have been treated in an Eulerian manner. Considering both these issues, the predictions can be considered to be acceptable (though not exact) for the purpose of developing insights into the effects of type of sparger and presence of draft tube. All the other simulations including the ones shown in Fig. 7b (partial sparging without draft tube) have been carried out with these parameters ($e = 0.95$, $\varepsilon_{smax} = 0.65$). These parameters are not fitted for each case. Predictions for all the remaining cases can then be considered to be a priori. Considering that there are no fitted parameters for this case, the predictive ability of the model can be considered to be adequate.

Taghipour et al. [2] have compared the model predictions with the experimental data and bed voidage. Their model was also able to qualitatively predict the experimental results. However, large errors were observed in the predictions. Errors as much as 30–50% in the prediction of bed voidage and pressure drops were reported. Pugsley and McKeen [6] have observed large errors between the predicted values of bed expansion and experimental measurements. In order to reduce the errors, the drag relationship was multiplied by an empirically fitted constant. The value of this constant was varied from 0.1 to 1.0. In spite of this, the predictions agree only qualitatively.

To understand the solid flow patterns and to examine the effects internals (draft tube) and distributor configuration (complete and partial sparging) on the hold-up distribution, CFD simulations were

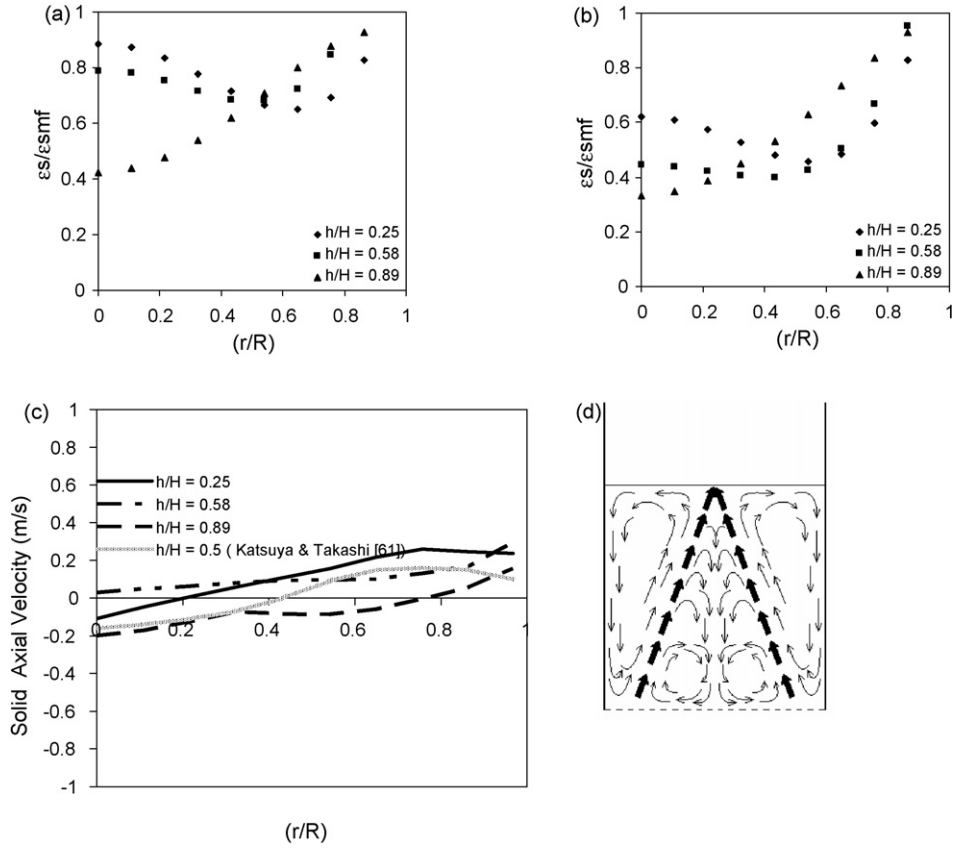

Fig. 8. Complete sparging without draft tube. (a) Solids hold-up profiles for $U_0/U_{mf} = 5.6$. (b) Solids hold-up profiles for $U_0/U_{mf} = 12.4$. (c) Solids axial velocity profiles. (d) Qualitative solids circulation patterns (thick arrows shows the air flow and thin arrows shows the solids flow).

carried out with the validated model for partial sparging with and without draft tube for U_0/U_{mf} of 12.4. The generated velocity profiles were used to examine the effect of sparging area and the draft tube on the solids circulations patterns.

4. Results and discussion

4.1. Complete sparging without draft tube

Fig. 8a shows the experimentally measured solids hold-up profile obtained for complete sparging without draft tube for U_0/U_{mf} of 5.6 for all axial locations (i.e., at h/H of 0.25, 0.58 and 0.89). At h/H of 0.25 (just above the distributor), high solid hold-up can be seen in the central region ($\varepsilon_s/\varepsilon_{smf}$ of approximately 0.9). At this location solid hold-up is lowest ($\varepsilon_s/\varepsilon_{smf}$ of approximately 0.6) at a radial location, $r/R = 0.6$. The solid hold-up further increases towards the wall. At h/H of 0.58 the solids hold-up profile is similar in shape to that of $h/H = 0.25$. However, the magnitude of solids hold-up in the central region is slightly lower and that near the wall, it is slightly higher. At h/H of 0.89 the solids hold-up profile is dramatically different in shape. The solids hold-up values continuously increase from center to wall. This indicates that at this location all the gas predominantly flows through the central region.

Fig. 8b shows the experimentally measured solids hold-up profiles obtained for complete sparging without draft tube for U_0/U_{mf} of 12.4 for all axial locations (i.e., at h/H of 0.25, 0.58 and 0.89). It can be seen that the hold-up profiles are similar in shape to the ones seen in Fig. 8a. However, all solids hold-up in the central region are lower. This is due to the higher superficial velocity leading to higher gas hold-up and consequently lower solids hold-up.

Fig. 8c shows the predicted solids axial velocity profiles obtained for complete sparging without draft tube for U_0/U_{mf} of 5.6 for all axial locations (i.e., at h/H of 0.25, 0.58 and 0.89). At h/H of 0.25 ($r/R < 0.2$) solid phase axial velocity is negative indicating that in the central region solids are flowing downward. At larger values of r/R the solids axial velocity is positive indicating that the solids are moving upwards. This indicates that solids are flowing upwards along with the gas (low solid hold-up, high gas hold-up at r/R of 0.6 (Fig. 8a and b) in this region. At h/H of 0.58, solid phase axial velocity is positive indicating upward flow of solids. At h/H of 0.89, solid phase axial velocity is downward. This is because, this location is close to the bed surface and this region is dominated by solid particles disengaging from gas and flowing down back into the bed. Figure also shows the solid axial velocities measured by Katsuya and Takashi [61] for their fluidized bed. Their experiments were for beds of similar size and operating under similar conditions to that used in our work. The solid velocities were measured by a fibre optic probe. It can be seen that at $h/H = 0.5$, the solid axial velocities measured by Katsuya and Takashi [61] are very similar to those of observed in our work at $h/H = 0.25$. The variation of velocity with radial distance is very similar to that observed by us. The small differences in solid velocities are in part due to different sparger details.

Fig. 8d shows the gas and solids flow patterns for complete sparging without draft tube for both U_0/U_{mf} of 5.6 and 12.4. At $h/H = 0.25$, the solids down flow is predominant in a stable central stream, within which there are nearly no bubbles. In addition, solids flow down along the walls, confined to very narrow band. The rest of the cross-section is utilized for the flow of gas. Katsuya and Takashi [61] observed that bubbles are generated in an annulus near the wall at the bottom of the bed and then come to the center as they rise to the center of the bed. Earlier [34], similar velocity profiles have been reported. The magnitudes of the solid velocities were in the range 0.05–0.1 m/s. This agrees well with our CFD model results.

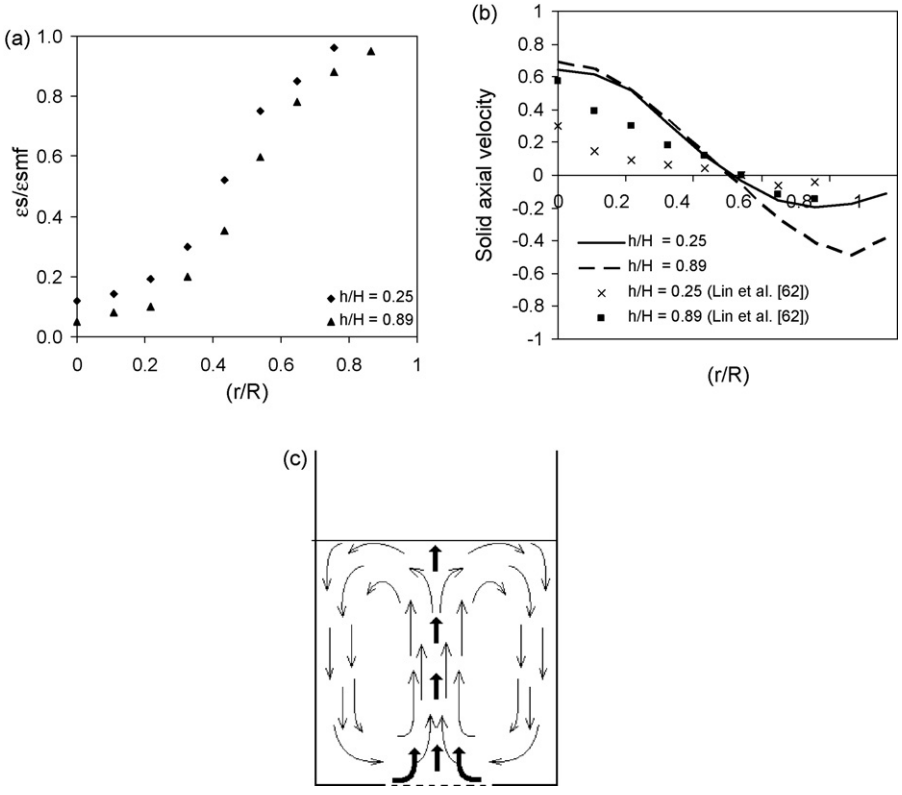

Fig. 9. Partial sparging without draft tube for $U_0/U_{mf} = 12.4$. (a) Solids hold-up profiles. (b) Solids axial velocity profiles. (c) Qualitative solids circulation patterns (thick arrows shows the air flow and thin arrows shows the solids flow).

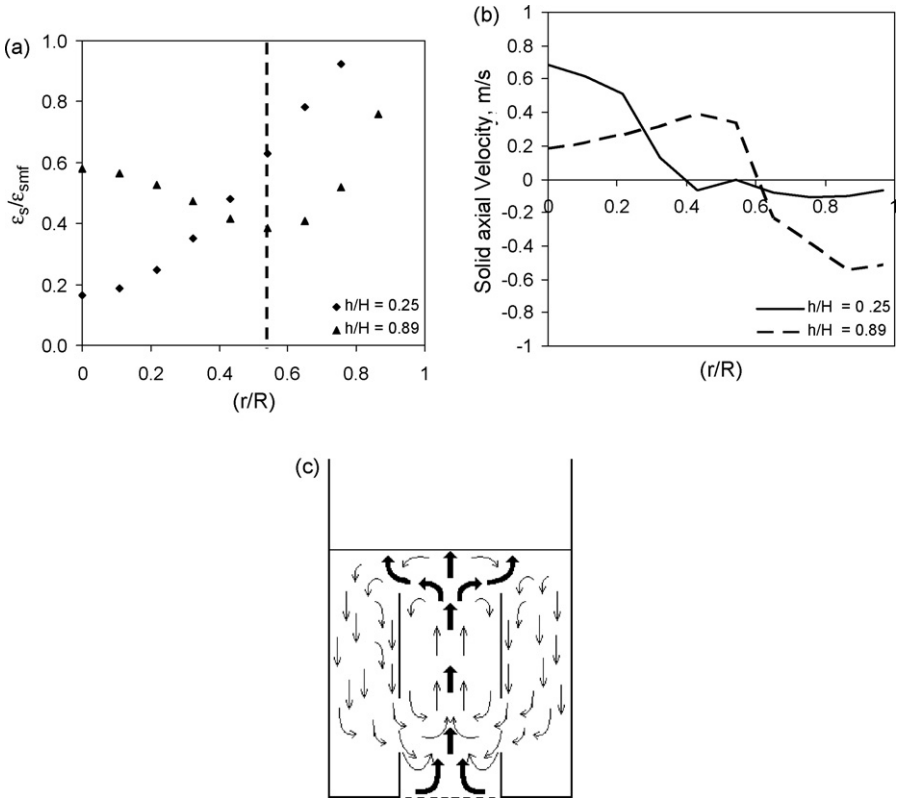

Fig. 10. Partial sparging with draft tube for U_0/U_{mf} = 12.4. (a) Solids hold-up profiles. (b) Solids axial velocity profiles. (c) Qualitative solids circulation patterns (thick arrows shows the air flow and thin arrows shows the solids flow).

4.2. Partial sparging without draft tube

Fig. 9a shows the experimentally measured solids hold-up profiles obtained for partial sparging without draft tube for U_0/U_{mf} of 12.4 and h/H of 0.25 and 0.89. At h/H of 0.25 (just above the distributor), the solids hold-up is lower at the centre region for partial sparging than compared to complete sparging without draft tube (Fig. 8b). This is because the gas is sparged through the center in case of partial sparging. This leads to higher gas hold-up and consequently lower solids hold-up in the central region. Solids hold-up are higher near the wall for partial sparging than that of complete sparging. At h/H of 0.89, it can be seen that the solids hold-up is lower in the case of partial sparging up to r/R of 0.54 (Figs. 9a and 8b). This is because in case of partial sparging, air passing through the sparged area (r/R from 0 to 0.54) is higher compared to complete sparging. For r/R greater than 0.54 up to the wall ($r/R = 0.85$) the solids hold-up was same irrespective of the type of sparging.

Fig. 9b shows the predicted solids axial velocity profiles obtained for partial sparging without draft tube for U_0/U_{mf} of 12.4 for h/H of 0.25 and 0.89. A well developed core annulus structure is observed in case of partial sparging without draft tube. The CFD prediction of solids axial velocity confirms the core annulus structure in case of partial sparging without draft tube (Fig. 9b). The solid phase axial velocity is positive indicating upward movement of solids through the sparged area (r/R from 0 to 0.54) for both h/H of 0.25 and 0.89 and down flow of solids takes place near the wall (for r/R greater than 0.54 up to the wall, $r/R = 0.85$). The solid axial velocities measured by Lin et al. [62] have also been plotted in this graph. They have measured the solid axial velocities by using Computer Aided Radio Particle Tracking (CARPT). Figure shows that the variation of solid axial velocities with radial location is similar to that observed by us. The magnitudes of the axial velocities are slightly lower than that observed by us. This could be in part due to the high gas velocity used in the present work as compared to that used by Lin et al. [62].

The qualitative flow patterns of gas and solids are shown in Fig. 9c. The up-flow of solids takes place with the gas at the center and there is predominant down flow of solids near the wall. The gas hold-up profile and the axial velocity profile show similar characteristics to the gas hold-up and liquid velocity profile in case of gas–liquid bubble columns operated in the heterogeneous regime.

4.3. Partial sparging with draft tube

Fig. 10a shows the solids hold-up profiles obtained for partial sparging with draft tube for U_0/U_{mf} of 12.4 and h/H of 0.25 and 0.89. At h/H of 0.25, solids hold-up increases with radial distance. In the central region, the solids hold-up values are lower for partial sparging as compared to complete sparging with draft tube (Figs. 10a and 8a). This is because, in case of partial sparging, most of the gas passes through the draft tube region. However, in the annular region ($r/R > 0.54$), solids hold-up is lower for complete sparging with draft tube (shown later) than for partial sparging with draft tube as gas is also sparged through the annulus in case of complete sparging. At h/H of 0.89, as the gas comes out of the draft, the plume of gas shifts radially towards the wall of the draft tube. As a result, the solid fraction is lower near the wall of the draft tube and higher in the central region. Close to column wall, the solids fraction is high because partial sparging together with draft tube practically ensures that practically no gas is present outside the draft tube.

Fig. 10b shows the predicted solids axial velocity profiles obtained for partial sparging with draft tube for U_0/U_{mf} of 12.4 at h/H of 0.25 and 0.89. At h/H of 0.25, for $r/R < 0.54$, solid phase axial velocity is positive indicating that in the central region solids are flowing upwards along with the gas. At larger values of r/R the

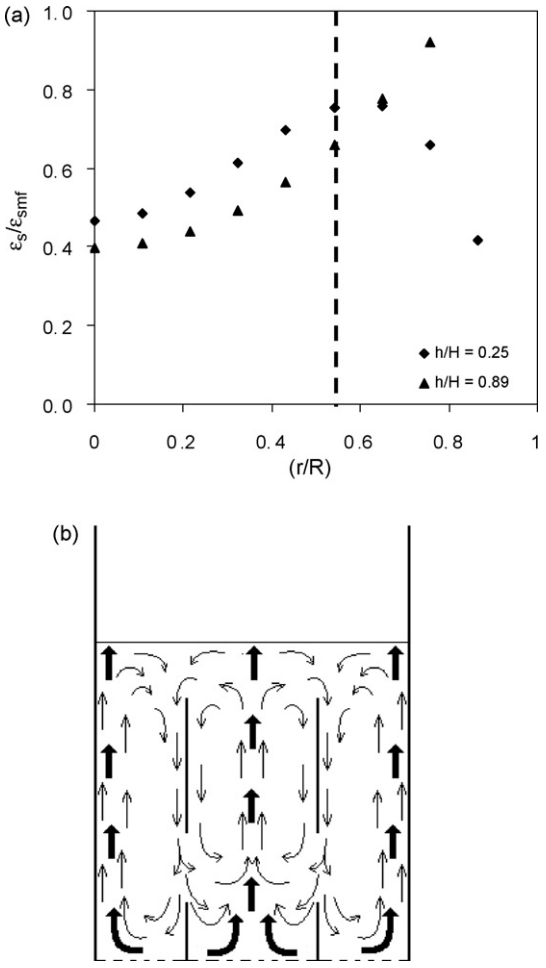

Fig. 11. Complete sparging with draft tube for U_0/U_{mf} = 12.4. (a) Solids hold-up profiles. (b) Qualitative solids circulation patterns (thick arrows shows the air flow and thin arrows shows the solids flow).

solids axial velocity is negative indicating that the solids are moving downwards. At h/H of 0.89 (up to r/R of 0.6), the solid phase axial velocity is higher indicating the solids are flowing upwards along with the gas (low solid hold-up, high gas hold-up, Fig. 10a). For higher values of r/R the solid phase axial velocity is negative indicating the solids are moving downward. Fig. 10c shows the qualitative gas and solids flow patterns for partial sparging with draft tube for U_0/U_{mf} of 12.4.

4.4. Complete sparging with draft tube

Fig. 11a shows the solids hold-up profiles obtained for complete sparging with draft tube for U_0/U_{mf} of 12.4 and h/H of 0.25 and 0.89. In this case (h/H = 0.25), solid hold-up patterns observed for both the draft tube region and the annulus region show an opposite trend as compared to complete sparging without draft tube (Figs. 11a and 8b). There is increase of solids hold-up up to r/R of 0.54 in case of complete sparging with draft tube, whereas there is decrease in the solids hold-up in case of complete sparging without draft tube. This is due to the introduction of the draft tube. Within the draft tube (up to r/R of 0.54), the solids hold-up is lower when draft tube is present. This is because majority of the sparged gas passes through the central region of the bed due to the presence of draft tube. A lower solids hold-up is observed in the annular region of the bed with the introduction of draft tube (Fig. 11a). This is because the gas sparged into the annular region, instead of moving towards the central region of the bed as seen in case of absence of draft tube, moves closer to the wall. At h/H of 0.89 (just above the draft tube and below the bed surface) (Figs. 11a and 8b), solid hold-up increases away from the centre for both the cases because the effect of draft tube is no longer pronounced.

Fig. 11b shows the qualitative gas and solids flow patterns for complete sparging with draft tube for both U_0/U_{mf} of 12.4. Majority of the sparged gas moves upwards through the central region of the bed due to the presence of draft tube. The upward flow of solids takes place along with the gas in the center and near the column walls and solids down-flow is along the walls of the draft tube.

La Nauze [63] studied the solids circulation pattern by using particle tracking method for a 0.3 m diameter air-sand internally circulating fluidized bed (with a draft tube). It was observed that the solids flow upwards through the draft tube and downward in the annulus.

5. Conclusions

The effects of superficial gas velocity, presence of draft tube and type of sparging on the solid hold-up and solid circulation patterns have been studied with the help of experiments and CFD simulations. A 2D multifluid Eulerian model integrating the kinetic theory of granular flows is developed. The predicted solids hold-up profiles agrees reasonably with the experimental data. The model is able to predict the hydrodynamic behavior of gas–solid fluidized beds. The type of sparging was found to have a dramatic effect on the solids hold-up profiles. In case of complete sparging without draft tube, the sparged gas traveled upwards near r/R = 0.6 close to sparger. Further away from the sparger, the gas moved to centre giving rise to up-flow of solids in the central region and down-flow near the walls. Partial sparging with and without draft tube leads to a well developed core annulus structure within the bed, similar to gas–liquid bubble columns operated in the heterogeneous regime.

References

[1] R. Krishna, J.M. van Baten, Using CFD for scaling up gas–solid bubbling fluidized bed reactors with Geldart A powders, Chemical Engineering Journal 82 (2001) 247–257.
[2] F. Taghipour, N. Ellis, C. Wong, Experimental and computational study of gas–solid fluidized bed hydrodynamics, Chemical Engineering Science 60 (2005) 6857–6867.
[3] M. Syamlal, T.J. O'Brien, Simulation of granular layer inversion in liquid fluidized-beds, International Journal of Multiphase Flow 14 (1988) 473–481.
[4] D. Gidaspow, Multiphase Flow and Fluidization, Academic Press, San Diego, 1994.
[5] C.Y. Wen, Y.H. Yu, Mechanism of fluidization. Chemical Engineering Progress Symposium Series, vol. 62, 1966, pp. 100–111.
[6] T. Pugsley, T. McKeen, Simulation and experimental validation of a freely bubbling bed of FCC catalyst, Powder Technology 129 (2003) 139–152.
[7] S. Ergun, Fluid flow through packed columns, Chemical Engineering Progress 48 (1952) 89–94.
[8] L.G. Gibilaro, R. Di Felice, S.P. Waldram, Generalized friction factor and drag coefficient correlations for fluid–particle interactions, Chemical Engineering Science 40 (1985) 1817–1823.
[9] R. Krishna, J.L. Sinclair, J.C. Schouten, B.G.M. van Wachem, C.M. van den Bleek, Comparative analysis of CFD models of dense gas–solid systems, AIChE Journal 47 (2001) 1035–1051.
[10] W. Du, X. Bao, J. Xu, W. Wei, Computational fluid dynamics (CFD) modeling of spouted bed: Assessment of drag coefficient correlations, Chemical Engineering Science 61 (2006) 1401–1420.
[11] K. Rietema, S.M.P. Mutsers, The effect of inter-particle forces on the expansions of a homogeneous gas-fluidized bed, in: Proc. Int. Symp. on Fluidization, Toulouse, 1973, p. 28.
[12] D. Gidaspow, B. Ettehadieh, Fluidization in two-dimensional beds with a jet. 2. Hydrodynamic modeling, Industrial & Engineering Chemistry Fundamentals 22 (1983) 193–201.
[13] B. Ettehadieh, D. Gidaspow, R.W. Lyczkowski, Hydrodynamics of Fluidization in a semicircular bed with a jet, AIChE Journal 30 (1984) 529.
[14] D. Gidaspow, Hydrodynamics of fluidization and heat transfer: supercomputer modeling, Applied Mechanical Review 39 (1986) 1.

[15] J.A.M. Kuipers, K.J. Van Duin, F.P.H. Van Beckum, W.P.M. Van Swaaji, A numerical model of gas-fluidized beds, Chemical Engineering Science 47 (1992) 1913–1924.
[16] J.X. Bouillard, R.W. Lyczkowski, S. Folga, D. Gidaspow, G.F. Berry, Hydrodynamics of erosion of heat exchanger tubes in fluidized bed combustors, Canadian Journal of Chemical Engineering 67 (1989) 218–229.
[17] H. Enwald, A.E. Almstedt, Fluid dynamics of a pressurized fluidized bed: comparison between numerical solutions from two-fluid models and experimental results, Chemical Engineering Science 54 (1999) 329–342.
[18] S. Chapman, T.G. Cowling, The Mathematical Theory of Non-uniform Gases, 3rd ed., Cambridge University Press, Cambridge, 1970.
[19] C.K.K. Lun, S.B. Savage, D.J. Jeffrey, N. Chepurniy, Kinetic theories for granular flow—inelastic particles in Couette-flow and slightly inelastic particles in a general flow field, Journal of Fluid Mechanics 140 (1984) 223–256.
[20] J. Ding, D. Gidaspow, A bubbling fluidization model using kinetic theory of granular flow, AIChE Journal 36 (1990) 523–538.
[21] J.M. Ding, R.W. Lyczkowski, Three-dimensional kinetic-theory modeling of hydrodynamics and erosion in fluidized-beds, Powder Technology 73 (1992) 127–138.
[22] C.C. Pain, S. Mansoorzadeh, C.R.E. de Oliveira, A study of bubbling and slugging fluidized beds using the two-fluid granular temperature model, International Journal of Multiphase Flow 27 (2001) 527–551.
[23] V.V. Ranade, R.P. Utikar, Single jet fluidized beds: experimental and CFD simulations with glass and polypropylene particles, Chemical Engineering Science 62 (2007) 167–183.
[24] J.A.M. Kuipers, D.J. Patil, M. van Sint Annaland, Critical comparison of hydrodynamics models for gas–solid fluidized beds—Part II: freely bubbling gas–solid fluidized beds, Chemical Engineering Science 60 (2005) 73–84.
[25] R. Krishna, J.C. Schouten, B.G.M. van Wachem, C.M. van den Bleek, Eulerian simulations of bubbling behavior in gas–solid fluidized beds, Computers and Chemical Engineering 22 (1998) S299–S306.
[26] A. Samuelsberg, B.H. Hjertager, An experimental and numerical study of flow patterns in circulating fluidized bed reactor, International Journal of Multiphase Flow 22 (1996) 575–591.
[27] K. Johansson, B.G.M. van Wachem, A.E. Almstedt, Experimental validation of CFD models for fluidized beds: influence of particle stress models, gas phase compressibility and air flow models, Chemical Engineering Science 61 (2006) 1705–2117.
[28] W. Lin, Y. Jin, F. Wei, Y. Guo, Y. Cheng, Modeling the hydrodynamics of downer reactors based on kinetic theory, Chemical Engineering Science 54 (1999) 2019–2027.
[29] J.R. Grace, F. Taghipour, Verification and validation of CFD models and dynamic similarity for fluidized beds, Powder Technology 139 (2004) 99–110.
[30] J.A.M. Kuipers, D.J. Patil, M. van Sint Annaland, Critical comparison of hydrodynamics models for gas–solid fluidized beds—Part I: bubbling gas–solid fluidized beds operated with a jet, Chemical Engineering Science 60 (2005) 57–72.
[31] R.C. Darton, R.D. LaNauxe, J.F. Davidson, D. Harrison, Bubble growth due to coalescence in fluidized beds, Transactions of the Institutions of Chemical Engineers 55 (1977) 274–280.
[32] K.S. Lim, V.S. Gururajan, P.K. Agrawal, Mixing of homogeneous solid in bubbling fluidized beds: theoretical modeling and experimental investigation using digital image analysis, Chemical Engineering Science 48 (1993) 2251–2265.
[33] K. Hilligardt, J. Werther, Local bubble gas hold-up and expansion of gas/solid fluidized beds, German Chemical Engineering 9 (1986) 215–221.
[34] S. Mori, R. Yamazaki, N. Kobayashi, A study on the behavior of bubbles and solids in bubbling fluidized beds, Powder Technology 113 (2000) 327–344.
[35] Y. Zhang, J.M. Reese, Continuum modeling of granular particle flow with inelastic inter-particle collisions, Transactions of the Institutions of Chemical Engineers 81 (2003) 483–488.
[36] J.J. Nieuwland, M. van Sint Annaland, J.A.M. Kuiper, W.P.M. van Swaaij, Hydrodynamics modelling of gas particle flows in riser reactors, AIChE Journal 42 (1996) 1569–1582.
[37] J.J. Nieuwland, R. Meijer, J.A.M. Kuiper, W.P.M. van Swaaij, Measurements of solid concentration and axial solids velocity in gas–solid two phase flow, Powder Technology 87 (1996) 127–139.
[38] B.G.M. van Wachem, J.C. Schouten, R. Krishna, C.M. van den Bleek, Validation of the Eulerian simulated dynamic behavior of gas–solid fluidized beds, Chemical Engineering Science 54 (1999) 2141–2149.
[39] A.P. Baskakov, V.G. Tuponogov, N.F. Filippovsky, A study of pressure fluctuations in a bubbling fluidized bed, Powder Technology 45 (1986) 113–117.
[40] J.C. Schouten, C.M. Van den Bleek, Chaotic hydrodynamics of fluidization: consequences for scaling and modeling of fluid bed reactors, AIChE Symposium Series 289 (1992) 780–784.
[41] J.C. Schouten, M.L.M. van der Stappen, C.M. van den Bleek, Scale-up of chaotic fluidized bed hydrodynamics, Chemical Engineering Science 51 (1996) 1991–2000.
[42] L. Cammarata, P. Lettieri, G.D.M. Micale, D. Colman, 2D and 3D CFD simulations of bubbling fluidized beds using Eulerian–Eulerian models, International Journal of Chemical Reaction Engineering 1 (2003) 48.
[43] I. Hulme, E. Clavelle, L. van der Lee, A. Kantzas, CFD modeling and validation of bubble properties for a bubbling fluidized bed, Industrial Engineering Chemistry Research 44 (2005) 4254–4266.
[44] I. Hulme, A. Kantzas, Validation of bubble properties of a bubbling fluidized bed reactor using CFD with imaging experiments, Polypropylene and Plastic Technology Engineering 44 (2005) 1–23.
[45] J.R. Grace, Canadian Journal of Chemical Engineering 64 (1986) 353.
[46] A.R. Thatte, R.S. Ghadge, A.W. Patwardhan, J.B. Joshi, G. Singh, Local gas holdup measurement in sparged and aerated tanks by γ ray attenuation technique, Industrial and Engineering Chemistry Research 43 (2004) 5389–5399.
[47] K.A. Shollenberger, J.R. Torzynski, D.R. Adkins, T.J. O'Hern, N.B. Jackson, Gamma-densitometry tomography of gas holdup spatial distribution in industrial-scale bubble columns, Chemical Engineering Science 52 (1997) 2037–2048.
[48] W.C. Mih, An empirical shear stress equation for general solid–fluid mixture flows, International Journal of Multiphase Flow 19 (1993) 683–690.
[49] Y.L. Yang, Y. Jin, Z.Q. Yu, J.X. Zhu, H.T. Bi, Local slip behaviors in the circulating fluidized bed, AIChE Symposium Series 296 (1993) 81–90.
[50] M. Syamlal, T.J. O'Brien, W. Rojers, MFIX Documentation volume 1, Theory Guide, 1993.
[51] A. Boemer, H. Qi, U. Renz, S. Vasquez, F. Boysan, Eulerian computation of fluidized bed hydrodynamics—a comparison of physical models, in: Proc. of the Int. Conf. on FBC, 1995, p. 775.
[52] A. Boemer, H. Qi, U. Renz, Eulerian simulation of bubble formation at a jet in a two-dimensional fluidized bed, International Journal of Multiphase Flow 23 (1997) 927–944.
[53] J.A.M. Kuipers, A two-fluid micro balance model for fluidized beds, Dissertation at the University of Twente, The Netherlands.
[54] C.M. Hrenya, J.L. Sinclair, Effect of particle phase turbulence in gas–solid flows, AIChE Journal 43 (1997) 853.
[55] D. Schaffer, Instability in the evolution equations describing incompressible granular flow, Journal of Differential Equations 66 (1987) 19–50.
[56] N.F. Carnahan, K.E. Starling, Equation of state for non-attracting rigid spheres, Journal of Chemical Physics 51 (1969) 635.
[57] C.K.K. Lun, S.B. Savage, The effects of impact velocity dependent coefficient of restitution on stress developed by sheared granular materials, Acta Mechanica 63 (1986) 15.
[58] J.L. Sinclair, R. Jackson, Gas-particle flow in vertical pipe with particle–particle interaction, AIChE Journal 35 (1989) 1473.
[59] H. Enwald, A.E. Almstedt, E. Peirano, Eulerian two-phase flow theory applied to fluidization, International Journal of Multiphase Flow 22 (1996) 21–66.
[60] D. Gidaspow, L. Huillin, Collision viscosity of FCC particles in a CFB, AIChE Journal 42 (9) (1996) 2503–2510.
[61] O. Katsuya, S. Takashi, in: D.L. Keairns (Ed.), Fluidization Technology, Hemisphere Publishing Corporation, Washington, 1976, pp. 95–110.
[62] J.S. Lin, M.M. Chen, B.T. Chao, A novel radioactive particle tracking facility for measurement of solids motion in gas fluidized beds, AIChE Journal 31 (3) (1986) 465–473.
[63] R.D. La Nauze, A circulation fluidized bed, Powder Technology 15 (1976) 117–127.
[64] K.G. Hansen, T. Solberg, B.H. Hjertager, A three-dimensional simulation of gas particle flow and ozone decomposition in the riser of a circulating fluidized bed, Chemical Engineering Science 59 (2004) 5217–5224.
[65] A. Sokolichin, G. Eigenberger, Applicability of the standard k-ε turbulence model to the dynamic simulation of bubble columns: Part I. Detailed numerical simulations, Chemical Engineering Science 54 (1999) 2273–2284.
[66] Y. John, P. Lettieri, G.D.M. Micale, L. Cammarata, CFD simulations of gas fluidized beds using alternative eulerian-eulerian modeling approaches, International Journal of Chemical Reactor Engineering 1 (2003) 1–19, Article A5.
[67] J. Ouyang, J. Li, Discrete simulations of heterogeneous structure and dynamic behavior in gas-solid Fluidization, Chemical Engineering Science 54 (1999) 5427–5440.
[68] C. Derek, P. Lettieri, G.D.M. Micale, L. Cammarata, 2D and 3D CFD simulations of gas fluidized beds using alternative eulerian-eulerian models, International Journal of Chemical Reactor Engineering 1 (2003) 1–19, Article A48.
[69] N. Yang, W. Wang, W. Ge, J. Li, CFD simulation of concurrent-up gas–solid flow in circulating fluidized beds with structure-dependent drag coefficient, Chemical Engineering Journal 96 (2003) 71–80.
[70] Y.P. Tsuo, D. Gidaspow, Computation of flow patterns in circulating fluidized beds, A.I.Ch.E. Journal 36 (6) (1990) 885–896.
[71] D.Z. Zhang, W.B. VanderHeyden, High-resolution three-dimensional numerical simulation of a circulating fluidized bed, Powder Technology 116 (2001) 133–141.
[72] D. Gera, M. Gautam, Y. Tsuji, T. Kawagchi, T. Tanaka, Computer simulation of bubbles in large particle fluidized beds, Powder Technology 98 (1998) 38–47.
[73] I.K. Gamwo, Y. Soong, W.R. Lyczkowski, Numerical simulation and experimental validation of solids flows in a bubbling fluidized beds, Powder Technology 103 (1999) 117–129.